Eur. Phys. J. B **18**, 363–369 (2000)

THE EUROPEAN
PHYSICAL JOURNAL B
EDP Sciences

Turbulence over arrays of obstacles in low temperature helium gas

H. Willaime[a], J. Maurer, F. Moisy, and P. Tabeling

Laboratoire de Physique Statistique, École Normale Supérieure, 24 rue Lhomond, 75231 Paris Cedex 05, France

Received 26 August 1999 and Received in final form 28 August 2000

Abstract. Turbulence produced in low temperature helium gas flowing over arrays of rectangular- and triangular-shaped blunt obstacles is investigated experimentally. The set-up allows both low fluctuation rates (down to 8%), and high microscale Reynolds numbers, R_λ (up to 1 150). The forced Kolmogorov equation is found to apply accurately. Similar to another flow configuration (counter rotating flow case [1]), the analysis of the flatness factor evolution with the Reynolds number reveals a transitional behavior around $R_\lambda \approx 650$.

PACS. 47.27.Gs Isotropic turbulence; homogeneous turbulence – 47.27.Jv High-Reynolds-number turbulence

1 Introduction

Using low temperature helium gas as the working fluid presents several advantages for the study of turbulence, compared to conventional systems. In particular, it offers the possibility to span a wide range of Reynolds numbers under controlled conditions. To date the largest value of the microscale Reynolds number, R_λ, achieved in a low temperature helium experiment is 5 040 [2,3], which is comfortably above the highest value ever attained in large wind tunnels. It is hoped that much higher values will be reached using larger low temperature helium facilities [4]. The range of variation of R_λ accessible in a single set-up with low temperature helium can be as large as thirty, which is again well beyond the best figures achieved with conventional fluids. Using low temperature helium thus potentially allows us to, under controlled conditions, address some issues, yet open, and lying at the core of the turbulence problem: is there any scaling at large Reynolds numbers? Do the small scales tend to be isotropic as the Reynolds number is increased? Is there a trend towards an asymptotic state, which could represent the infinite Reynolds number limit?

In the low temperature experiments mentioned in reference [3], the flow was driven by counter-rotating disks, equipped with blades. The measurements were performed at a single point, in the upper part of the circular mixing layer sustained by the counter-rotating disks. We now have an abundant set of data from this system. Perhaps the most surprising observation made was the existence of a transitional behavior in the evolution of the flatness factor of the velocity derivatives with R_λ. This transition was seen for $R_\lambda \approx 650$, a rather large value. Consistency with the latest available compilation of flatness factors [5] was shown [1]. We suggested that the difference between our set of measurements and those published by other investigators is that we identify a transition around $R_\lambda = 650$, where compiled data are too scattered to allow a firm conclusion. Note however that recent data obtained by Antonia [6] suggest, within their error bars, no transition. Tests have been made to detect possible probe effects in our experiment [7], but no artifact have been convincingly found. It was suggested that such a transition signals an instability of the worms (defined as the vortex tubes which retain the highest vorticity levels), and further conjectured that other transitions may take place at higher Reynolds numbers [8]. Since the observation was made in a particular and perhaps unconventional flow geometry, the issue was raised as to whether such a transition is limited to a particular flow geometry or whether it is a general property of all turbulent flows. It would be desirable indeed that accurate measurements were performed in conventional systems, so this can be clarified. However, this is an extremely difficult task and to the best of our knowledge, no real attempt is planned at the moment. On the other hand, numerical simulations are still far from being in position to tackle the problem. We thus decided to investigate another flow geometry, using again low temperature helium gas. The configuration we have chosen is a flow over a series of blunt obstacles. Apart from the transition issue, the experiment allows us to explore new flow configurations, in the context of low temperature helium turbulence.

---

[a] e-mail: `willaime@physique.ens.fr`

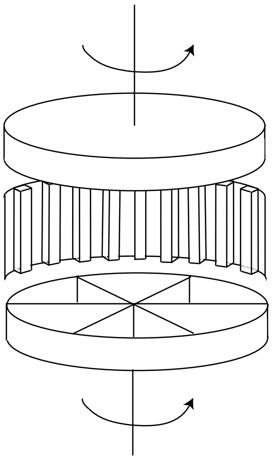

Fig. 1. Sketch of the cell.

2 Experimental set-up

The flow we consider here is sketched in Figure 1. It is driven between two coaxial disks, equipped with blades, similar to the ones used in reference [3]. The disks rotate at the same frequency and in the same direction. Far from the wall and the central axis, the flow resembles to a rigid-body rotation. Turbulence is produced by the flow past an array of blunt obstacles, mounted on the inner surface of the cylinder, in the central region. Two shapes have been used: square bars and triangular shaped obstacles. The square bars, placed in the large cell, are shown on Figures 1 and 2. They are 0.5 cm wide, 6 cm long and are placed with a 1 cm separation. In this system, the working fluid region is located between the two coaxial disks with 10 cm radius, spaced 13 cm apart. The other set of obstacles, placed in the smaller cell, are 8 triangles of base 1.4 cm, height 0.5 cm and thickness 0.05 cm, radially mounted on the periphery every 3.3 cm. The working region in this smaller cell is located between two disks with 3 cm radius, spaced 6 cm apart. In both cases, the cells are enclosed in cylindrical vessels, immersed in liquid helium bath at atmospheric pressure and 4.2 K. The vessels are filled with helium gas, held at a controlled pressure, and maintained at a fixed temperature between 4.2 and 6.5 K; the temperature is controlled with a long term stability better than 1 mK. Pressure and temperature are measured within 1% accuracy. All these characteristics allow us to operate in well controlled conditions.

We use "hot" wire probes to measure the turbulent fluctuations. The probes are of the same type as those described in reference [3]. The sensors are made from a 7 μm thick carbon fiber, stretched across a rigid frame; a metallic layer covers the fiber everywhere except on a spot at the center, 7 μm long, which defines the active length of the probes. The time responses of the probes are analyzed, in some detail, in reference [3].

We use two probes, one mobile and the other fixed. The mobile probe is displaced by using a step motor (Escap P310), located outside the cylindrical vessel enclosing the working fluid region. The elementary displacement is 0.05 mm, and the maximal separation from the wall is 5 cm. It is thus possible to make measurements at different locations, from just next to the wall and up to 5 cm from it, so as to characterize the large scale flow structure. The fixed probe is located 16 mm from the wall.

Fig. 2. Picture representing the fixed probe and the inner wall of the cylinder in which the flow takes place, on which the series of square bars is fixed.

Table 1 shows a representative set of experimental conditions we have studied. This covers only a fraction of the data sets we have (the total number is 50). In this table, the microscale Reynolds number is defined by:

$$R_\lambda = \frac{u'\lambda}{\nu},$$

where u' is the fluctuation of the longitudinal velocity, λ the Taylor microscale, and ν the kinematic viscosity. The Taylor and Kolmogorov scales are defined by $\lambda = u'(15\nu/\epsilon)^{1/2}$ and $\eta = (\nu^3/\epsilon)^{1/4}$. To determine the dissipation energy, ϵ, we consider the forced Kolmogorov equation (see part 4). The range of R_λ we address extends from 200 to 1 150 for the larger cell and from 100 to 800 in the smaller one; the fluctuation rate u'/U (where U is the local mean velocity) lies between 8 and 18% in the larger cell, but most of the files we analyze correspond to fluctuation rates around 10% (see Tab. 1). These figures are a factor of two below previous studies, using counter-rotating disks. We thus work with low fluctuation rates, at the expense of not reaching quite as high Reynolds numbers. We typically resolve the Kolmogorov scale for R_λ up to 700, and three times this scale at the highest Reynolds number. The resolution of the flatness factor in such cases will be discussed later.

3 Large scale characteristics of the flow

In the larger cell, the large scale structure of the flow has been investigated using the mobile probe described above. The evolution of the mean velocity and the longitudinal velocity fluctuations as a function of y, the distance from the wall, are shown in Figure 3. The measurements are restricted to a domain limited by $y \geq 0.8$ cm; below this value, the probe reaches the bars. One sees that the mean velocity, as expected, decreases as we get closer to the wall and drops off very fast within the last mm. The fluctuation rate u'/U, shown in the inset, is found to increase

Table 1. Typical experimental parameters: CL and R stand for the large system, using square bars and J for the small one, using triangular shaped obstacles.

file	$\nu \times 10^4$ (cm^2/s)	U (cm/s)	u' (cm/s)	u'/U	R_λ	η (μm)
1CL	7.6	60.4	6.50	0.18	558	14
4CL	7.6	176	17.9	0.10	1116	4.75
8CL	5	104.8	11.9	0.11	823	6.12
19CL	26.7	45	3.8	0.084	632	9.4
39CL	9.5	90.5	8.8	0.098	522	13.5
45CL	9.5	73.5	9.25	0.13	442	16.8
55CL	9.5	129	12.4	0.104	542	9.06
14R	8	33.2	4.9	0.15	283	15.8
22R	8	190	17.8	0.094	785	5.9
166J	16.7	30	6	0.20	242	22
209J	8	78	16	0.20	448	8.1

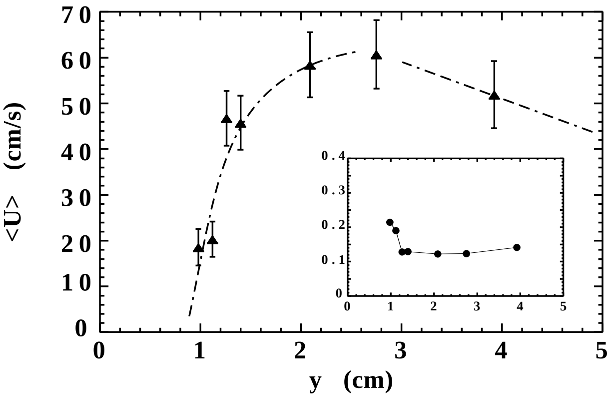

Fig. 3. Mean (filled triangles) and fluctuation (error bars) velocity profiles, as a function of the distance to the wall, y; the dashed lines are guides to the eyes (see text). The inset shows the fluctuation rate u'/U as a function of y.

as y decreases. For $y > 3$ cm, the mean velocity tends to decrease (indicated by the straight dashed line), as expected for a rigid-body rotation, with $U_\theta \approx \Omega(R-y)$ (where Ω is the angular velocity and R, the cell radius). An interesting aspect of the large scale structure, from our perspective, is that we can work with low fluctuation rates (down to 12% in this case), a figure appreciably smaller than the counter-rotating situation. The data sets in Table 1 have been obtained with the fixed probe, 16 mm from the wall, near the maximum of the velocity profile.

Another interesting characteristic is the probability density function (pdf) of the velocity. A representative example is shown in Figure 4 (55CL). For reasons difficult to figure out, the distributions show deviations from Gaussianity, and suggest the presence of exponential tails. This has to be compared with other flow configurations, where pdfs are found to be closer to Gaussian [3]. The main concern here is not the existence of such deviations, but rather to verify that there are no pathologies (such as bumps, or bimodality), in the statistics of the velocity fluctuations at large scales. This appears to be the case.

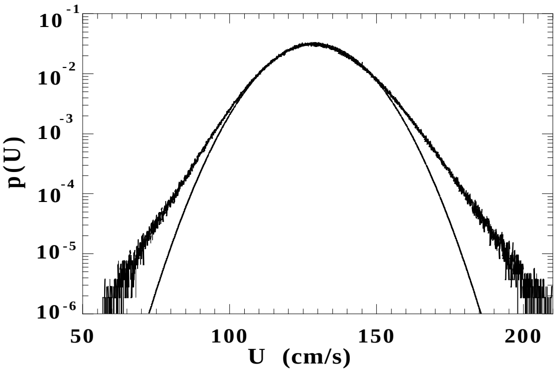

Fig. 4. pdf of the velocity fluctuations for file 55CL; the mean velocity is 129 cm/s, and the fluctuation rate is 10.4%. The full line is a Gaussian fit.

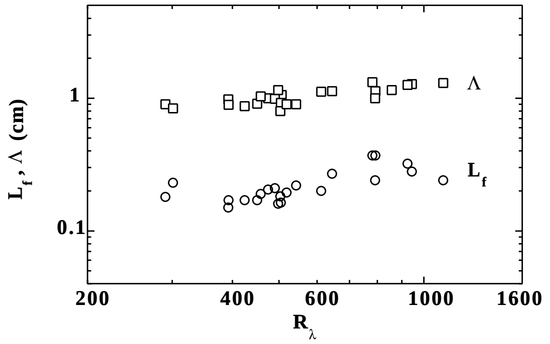

Fig. 5. Evolution of Λ and L_{f} in function of R_λ obtained in the larger cell.

The integral scale, Λ, is worth being mentioned here. It is defined by the velocity autocorrelation function through the relation:

$$\Lambda = \frac{1}{u'^2}\int_0^\infty \langle u(x)u(x+r)\rangle \,\mathrm{d}r, \qquad (1)$$

in which u is the zero mean fluctuation velocity, time is converted into distance by using Taylor hypothesis, and the brackets mean spatial average. In Figure 5, the evolution of Λ is plotted as a function of R_λ in the large cell case: as expected, no evolution is seen and $\Lambda = 1.05 \pm 0.15$ cm. For the small cell we obtain $\Lambda = 0.47 \pm 0.05$ cm. It is difficult to provide a precise interpretation of these measurements. In both cells, a plausible candidate for the integral scale is the typical size of the forcing (periodicity or height of the obstacles).

4 Energy spectrum and forced Kolmogorov equation

In order to identify possible artifacts in the signal, we analyze the turbulent spectrum and appreciate the quality of the signal in terms of signal to noise ratio. Figure 6 shows such an energy spectrum obtained with the fixed probe, at $R_\lambda = 672$ (file 39CL). One obtains the expected shape, *i.e.* a power law in a region of scales separated

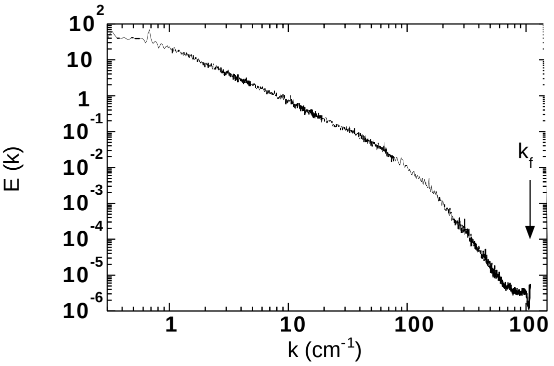

Fig. 6. Energy spectrum for file 39CL, for $R_\lambda = 672$; k_f is the filter wave-number.

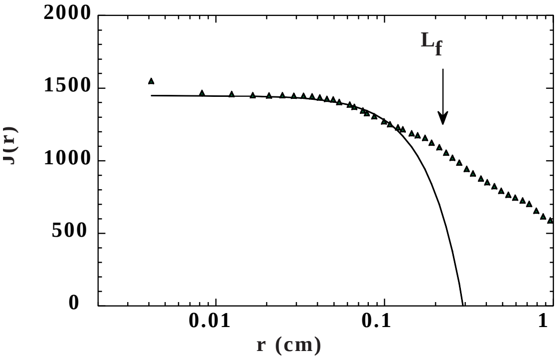

Fig. 7. Function $J(r)$ for file 55CL, $R_\lambda = 542$.

by the large scale forcing (signalled here by a peak at six times the rotation frequency of the disks), and the dissipative range. The sampling frequency (30 kHz) and the probe wave-number, $1/l_\mathrm{w}$ (1 500 cm^{-1}, where l_w is the active sensor length), are out of scale, and the low pass filter frequency, at 14 kHz, placed between the electronics and the data processing system, is indicated by an arrow on the spectrum. One sees in this particular case that the signal to noise ratio is comfortable (over 70 dB) and the various limiting factors do not prevent analyzing the fluctuations down to the dissipation scale. Such a situation is typical for Reynolds numbers up to 1 150. Above this value, we cease to resolve the dissipative range.

Again in view of analyzing the signal we have plotted the function, $J(r)$, defined by:

$$J(r) = -\frac{S_3}{r} + \frac{6\nu}{r}\frac{\mathrm{d}S_2}{\mathrm{d}r}, \tag{2}$$

in which S_3 is the third order longitudinal structure function, defined by:

$$S_p(r) = \langle (u(x+r) - u(x))^p \rangle, \tag{3}$$

with p=3. It is interesting to introduce $J(r)$, because in the case of homogeneous, isotropic turbulence, this function is known to verify the following relation [9–11]:

$$J(r) = \frac{4}{5}\epsilon\left(1 - \frac{5}{14}\frac{r^2}{L_\mathrm{f}^2}\right), \tag{4}$$

where ϵ is the dissipation rate, and L_f is the effective forcing scale. We follow here a notation introduced by Novikov [11]. The relation is exact when isotropy and homogeneity hold, and when the forcing is applied at large scales. We called it the "forced Kolmogorov equation" according to reference [12]. ϵ and L_f are not known *a priori*, and using the above relation allows an accurate determination of them.

We have compared the experimental measurement of $J(r)$ with formula (4), and the result is shown in Figure 7 which is a linear-logarithmic plot. One sees the theoretical expression (4) provides an acceptable representation for the measurements, in a range of scales from 2×10^{-3} cm to 0.15 cm, *i.e.* almost two decades. Equation (4) becomes inappropriate above 0.15 cm, suggesting that the hypotheses under which it was derived (*i.e.* essentially isotropy and large scale forcing) ceases to apply. The forcing scale, L_f, we find with this approach, is 0.22 cm for file 55CL, a quantity well below the integral scale, Λ (1.05 cm). We obtain the following value for the larger set-up:

$$L_\mathrm{f} = 0.23 \pm 0.07 \text{ cm}$$

and for the smaller one:

$$L_\mathrm{f} = 0.19 \pm 0.02 \text{ cm}.$$

As there is no relation between equations (1) and (4), there is no reason for L_f and Λ to be equal. However, we expect, on physical grounds, that they have the same scaling as functions of the Reynolds number. These two scales are plotted in Figure 5. One can see that they can be indeed considered as constants for this range of R_λ, although a slight increase of L_f with R_λ can not be ruled out from these data. This may suggest that the forcing here acts at a slightly higher effective scale for larger R_λ.

It is worth pointing out that L_f is smaller than Λ. L_f is an effective forcing scale, below which the flow can be considered to be well described by the Kolmogorov equation, which requires homogeneity and isotropy. It is interesting to note that such a difference between Λ and L_f did not appear in previous experiments performed with counter-rotating disks [12]: for such experiments, the two scales were found to be indistinguishable. This suggests perhaps such scales are sensitive to different aspects of the system. Since it is plausible that L_f is more sensitive to the forcing than the integral scale, their ratio may probably be used, in general, to characterize the efficiency of the forcing to generate isotropic flow. We conclude that, in these experiments of turbulence over array of obstacles, the effective forcing scale is much lower than in experiments where disks are counter-rotating.

Note also that for several files, we have observed that the plateau is poorly defined; this is mostly due to the presence of a bump, whose amplitude may reach 20% of the plateau level. Such bumps are not systematic, and certainly signal the presence of a source of noise (vibrations, electromagnetic perturbations...), hard to identify in practice. Such bumps are well visible on the third order structure function, while often barely detectable on the spectrum. We actually have used the theoretical expression of ϵ from equation (4) to determine R_λ in all cases.

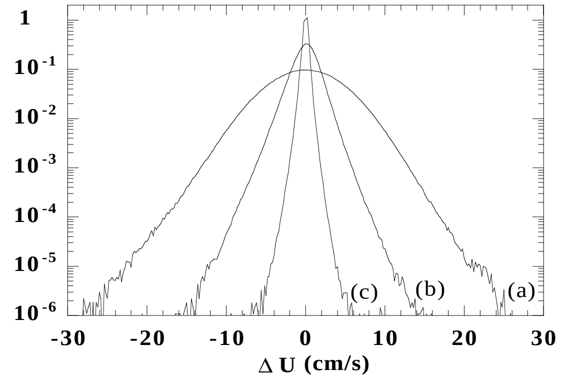

Fig. 8. Distributions of velocity increments for file 10CL, at $R_\lambda = 763$, and $\eta = 11.40$ μm; the separations are (a) $6\,000\eta$, (b) 60η, (c) 6η.

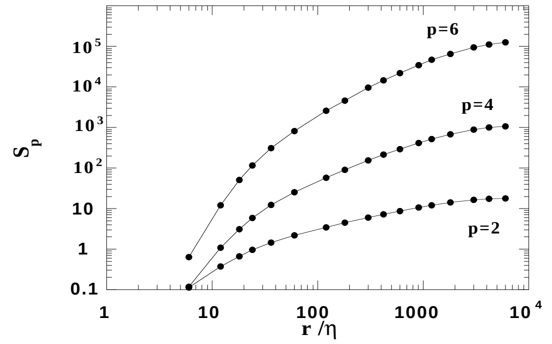

Fig. 9. Structure functions of order 2,4,6 for file 10CL; on the ordinate axis, the unit is $(\text{cm/s})^p$; the lines are drawn to guide the eyes.

5 Inertial range intermittency

It is worth analyzing the small scale intermittency of our turbulent flow, in the inertial range, by using the usual diagnostics, *i.e.* measuring pdfs of velocity increments at different scales, and the associated structure functions. They are presented in Figures 8 and 9 for $R_\lambda = 763$ (file 10CL).

In Figure 8, one sees that the pdfs of the velocity increments become broader as we approach the dissipative range, a well known evolution for three dimensional flows. The evolution of such distributions can be characterized by inspecting the structure functions, $S_p(r)$, some of which are shown in Figure 9, for the same R_λ. Again, one distinguishes three ranges of scale — dissipative at small r, inertial between $r/\eta \approx 20$ and $r/\eta \approx 2\,000$, and large scale beyond. In the inertial domain, a power law is a plausible, albeit inaccurate, representation of the structure functions. We suggest here, for the particular set-up we investigate, that there is insufficient scale separation to expect power law behavior of the structure functions. The regimes we examine here are such that the Kolmogorov function does not show a plateau which may explain that power laws do not accurately hold. Such an explanation may indeed not apply at extremely large Reynolds numbers [13].

The difficulties of defining structure function exponents vanish once relative exponents, obtained by the so called Extended Self Similarity [14], is used. The corresponding values of the exponents, for the absolute values of the increments, are shown in Figure 10. Here again, our system displays characteristics close to those found in other flow configurations [15].

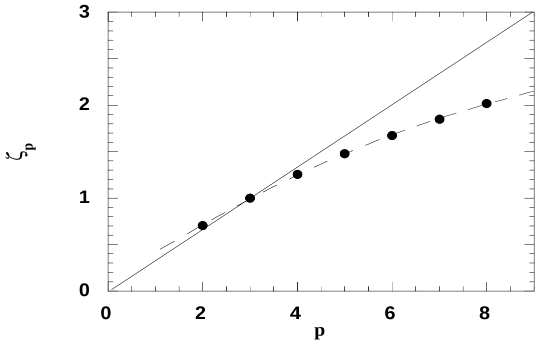

Fig. 10. Structure functions exponents for files 5-15CL. The straight line is Kolmogorov expectation and the dashed curve represents usual values obtained in other configurations.

6 Analysis of the intense longitudinal gradients

In this section, we focus on the intense longitudinal gradients, and in particular on the associated "structures" that we have identified as worms. A previous study of such events has been made in references [16,17]. As the procedure has been described in the quoted papers, we only recall the main points here.

We assume that the intense gradients are produced by the sweeping of vortex tubes across the probe. In particular, we have checked in reference [16] that the effect of a Burger-like vortex on the probe is consistent with the general shape of high gradient structures [17]. We present the result of the analysis, of file 55CL, corresponding to $R_\lambda = 542$. To identify the high gradient events, we consider the pdf of the velocity derivative and we focus on the events for which $|\mathrm{d}u/\mathrm{d}x| > 5.6$ times the standard deviation of the pdf, this threshold selects a small fraction of the signal (5%). Once the events occurring on the tails of the pdf of the velocity derivative are identified, one can measure their amplitude and their size. To perform this measurements, the two local extrema around the gradient are localized, and the peak to peak distance (resp. amplitude) gives the measurements of the size (resp. azimuthal velocity) of the events. Figures 11 and 12 show the distributions of the sizes and amplitudes of the worms we may associate with the large gradients. These distributions can be well fitted by lognormal distributions, which is consistent with previous observations. The mean radius of the worms is 3.7 η and their mean amplitude is 1.5 u', two values again consistent with previous estimates [16]. We see here that worms can be singled out from the time series, with the same properties as those obtained in other situations. This confirms their general relevance.

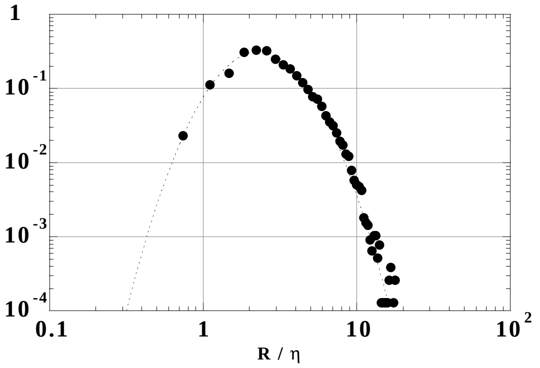

Fig. 11. Distribution of the size R of the worms, for file 55CL, *i.e.* for $R_\lambda = 542$.

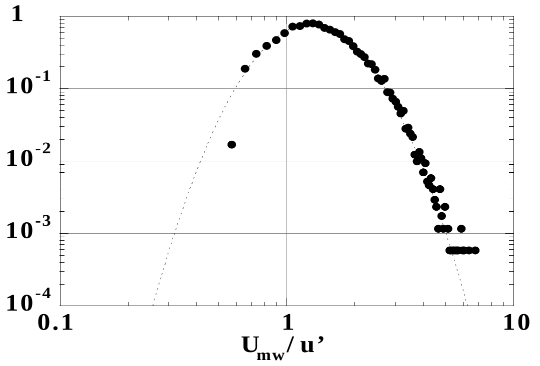

Fig. 12. Distribution of the amplitude U_{mw} of the worms for file 55CL, *i.e.* for $R_\lambda = 542$.

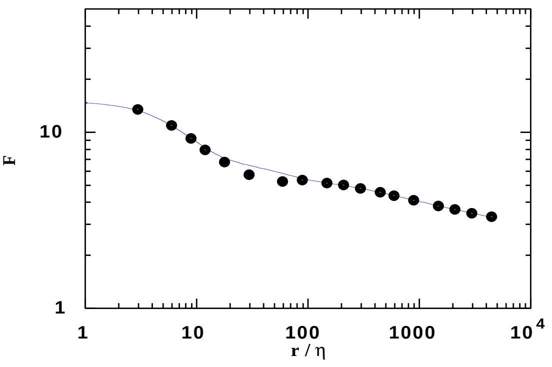

Fig. 13. Flatness factor for file 4CL, *i.e.* for $R_\lambda = 1116$. The full line is drawn to guide the eyes.

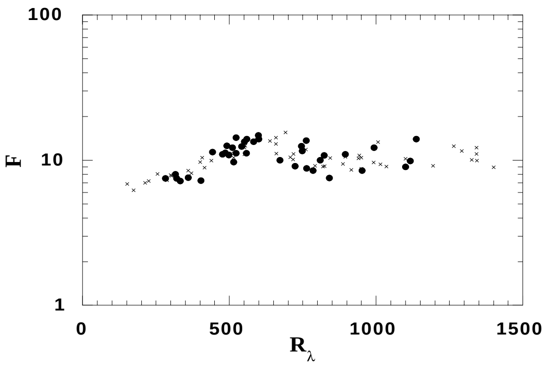

Fig. 14. Flatness of the velocity derivatives *vs.* R_λ. (●): present series of measurements. (×): earlier measurements, made with counter-rotating disks [1].

7 Dissipative range intermittency

Here we come to an issue, central in the discussions on dissipative range intermittency: the evolution of the flatness of the velocity derivatives as a function of R_λ. The flatness of the longitudinal increment $F(r)$ is defined by:

$$F(r) = \frac{S_4(r)}{(S_2(r))^2} \cdot \qquad (5)$$

We present in Figure 13 the evolution of $F(r)$ as a function of the separation r for one of the highest R_λ we could achieve ($R_\lambda = 1\,116$, file 4CL). One sees that $F(r)$ increases as r decreases, signalling the presence of internal intermittency. In the present case, the smallest scale we resolve is 3 η. To infer the flatness of the velocity derivative from this plot (labeled F), we make a quadratic extrapolation of the curve, assuming it levels off as r goes to zero. This procedure is unnecessary when the saturation is clearly visible, *i.e.* up to $R_\lambda = 700$. It becomes unavoidable at larger R_λ. The corresponding uncertainty increases with R_λ; we estimate it to be on the order of 15% up to R_λ =1 000 and roughly 20% for the highest Reynolds numbers we achieved.

We have carefully examined the statistical convergence of our flatness measurements. Convergence becomes an issue for the smaller separation, as R_λ increases beyond 900. Indeed, for high R_λ, as the tails of the distribution get wider, more statistics are needed to compute the moments of a given order. Here again, the level of uncertainty we can infer from this analysis, added to the previous one, is on the order of 25% for the largest R_λ we could reach.

The results, obtained as explained above, are displayed in Figure 14. One sees that F increases up to $R_\lambda \approx 600$ and tends to saturate, between 700 and 1 000, at a lower level. This suggests that a transition occurs around, say, $R_\lambda \approx 650$, consistently with previous measurements made in the counter-rotating system [1]. In order to check that this saturation does not come from the extrapolation of $F(r)$ for $r \to 0$, it is interesting to note that the flatness of the velocity increments for a separation scale of 3 η to 8 η also displays the same transitional behaviour around $R_\lambda \approx 650$. These quantities are interesting to consider, because their statistical convergence are easier to achieve, and no extrapolation is involved. The fact that we obtain the same evolution for the increments and the derivative strengthens the existence of a transitional behaviour and indicates that it contaminates a substantial part of the dissipative range. The present measurements of F, together with the ones obtained in the counter-rotating case, are shown in Figure 14: the evolutions of the flatness as a function of R_λ in these two configurations are the same. The consistency between the two sets of measurements is worth being pointed out.

8 Conclusion

In conclusion, we have made the following observations:

- Forced Kolmogorov equation is shown to apply; from it, an effective forcing scale L_f can be defined. This scale turns out to be well below the integral scale for our series of experiments; its low value may explain why scaling laws are not accurately observed in our case. We suggest that the effective forcing scale, L_f, is an important quantity to measure since it determines the range of scales within which, from inspection of the forced Kolmogorov relation, turbulence can be considered homogeneous and isotropic. The scales between L_f and Λ are probably affected by the large scale structure of the flow. We believe that L_f should be systematically taken into account in the discussion of the origin of the deviations from pure scaling laws in the inertial range. We also suggest that the ratio L_f/Λ provides a diagnostic on the efficiency of the forcing to generate isotropic turbulence.

- The intense longitudinal gradients have a structure similar to the one obtained in previous studies. If such events are associated to the sweeping of vortex tubes across the probe, then the characteristics of such tubes are the same as in previous experiments: their core size is around 3-4 η and the velocity difference is of the order of u'. These observations are also found to be in good agreement with numerical simulations [18].

- The flatness of the velocity derivatives shows a transitional behavior around $R_\lambda \approx 650$, consistent with previous investigations in the helium experiment [1]. This observation raises the issue of the general relevance of such a transition. At the moment, we don't know what to think about it.

This work has been supported by École Normale Supérieure, CNRS, the Universities Paris 6 and Paris 7 and by EEC Network Contract FMRX-CT98-0175. The authors thank J.S. Anderson for his helpful work.

References

1. H. Willaime, F. Belin, P. Tabeling, Eur. J. Mech. B **17**, 489 (1998).
2. G. Zocchi, P. Tabeling, J. Maurer, H. Willaime, Phys. Rev. E **50**, 3693 (1994).
3. P. Tabeling, G. Zocchi, F. Belin, J. Maurer, H. Willaime, Phys. Rev. E **53**, 1613 (1996).
4. *Flows at Ultra-High Reynolds and Rayleigh numbers, a status report*, edited by R.J. Donnelly, K.R. Sreenivasan (Springer, 1998).
5. K.R. Sreenivasan, R.A. Antonia, Annu. Rev. Fluid Mech. **29**, 435 (1997).
6. B. Antonia, B. Pearson, private communication (2000).
7. V. Emsellem, L.P. Kadanoff, D. Lohse, P. Tabeling, Z.J. Wang, Phys. Rev. E **55**, 2672 (1997).
8. F. Belin, J. Maurer, H. Willaime, P. Tabeling, Phys. Fluids **9**, 3843 (1997).
9. A detailed presentation of the equation can be found in A.S. Monin, A.M. Yaglom, *Statistical Fluid Mechanics* (MIT Press, Cambridge, MA, 1975), Vol. 2.
10. A.N. Kolmogorov, Dokl. Akad. Nauk. SSSR **32**, 16 (1941) [Proc. R. Soc. Lond. A **434**, 15 (1991)].
11. E.A. Novikov, Zh. Exper. Teor. Fiz. **47**, 1919 (1964) [Sov. Phys. JETP **20**, 1290 (1965)].
12. F. Moisy, P. Tabeling, H. Willaime, Phys. Rev. Lett. **82**, 3994 (1999).
13. K.R. Sreenivasan, B. Dhruva, Prog. Theor. Phys. Suppl. **130**, 103 (1998).
14. R. Benzi *et al.*, Phys. Rev. E **48**, R29 (1993).
15. A. Arneodo *et al.*, Europhys. Lett. **34**, 411 (1996).
16. F. Belin, J. Maurer, P. Tabeling, H. Willaime, J. Phys. II France **6**, 573 (1996).
17. F. Belin, F. Moisy, P. Tabeling, H. Willaime, Trends in Mathematics, 129 (1999).
18. J. Jimenez, Eur. J. Mech. B **17**, 405 (1998).